PNAS RESEARCH ARTICLE | CHEMISTRY

Magnet-in-ferroelectric crystals exhibiting photomultiferroicity

Zhongxuan Wang[a], Qian Wang[b], Weiyi Gong[c], Amy Chen[a], Abdullah Islam[a], Lina Quan[b,d], Taylor J. Woehl[e], Qimin Yan[c], and Shenqiang Ren[a,1]

Edited by Thomas Mallouk, University of Pennsylvania, Philadelphia, PA; received December 27, 2023; accepted March 18, 2024

Growing crystallographically incommensurate and dissimilar organic materials is fundamentally intriguing but challenging for the prominent cross-correlation phenomenon enabling unique magnetic, electronic, and optical functionalities. Here, we report the growth of molecular layered magnet-in-ferroelectric crystals, demonstrating photomanipulation of interfacial ferroic coupling. The heterocrystals exhibit striking photomagnetization and magnetoelectricity, resulting in photomultiferroic coupling and complete change of their color while inheriting ferroelectricity and magnetism from the parent phases. Under a light illumination, ferromagnetic resonance shifts of 910 Oe are observed in heterocrystals while showing a magnetization change of 0.015 emu/g. In addition, a noticeable magnetization change (8% of magnetization at a 1,000 Oe external field) in the vicinity of ferro-to-paraelectric transition is observed. The mechanistic electric-field-dependent studies suggest the photoinduced ferroelectric field effect responsible for the tailoring of photo-piezo-magnetism. The crystallographic analyses further evidence the lattice coupling of a magnet-in-ferroelectric heterocrystal system.

magnet-in-ferroelectrics | molecular ferroelectrics | magnetoelectrics

Significance

The coupling phenomena among photon, dipole, and spin in molecular materials have garnered considerable attention. Achieving the cross-correlation phenomenon between degrees of freedom through molecular crystal growth remains challenging. In this study, we demonstrate molecular magnet-in-ferroelectric with the coexistence of magnetism and ferroelectricity. This provides a pathway of photo-induced interfacial ferroelectric and magnetic coupling, offering the insights into photomultiferroic effects in molecular materials.

The coexistence and coupling of magnetic and electric degrees of freedom have stimulated ever-increasing attention in ultralow power memory, spin-filters, resonators, antenna, and terahertz emitters (1–6). The key to tailoring magnetism through the magnetoelectric effect lies in combining materials with distinct magnetic and electric order while triggering the "product" property at the cohesive interface between adjacent ferroelectro-magnet materials (2, 7–9). Photoswitchable magnetism, the so-called photomagnetism, provides a complementary noncontact avenue for tailoring magnetic properties in the reversible manner. An interest arises if photomagnetoelectricity could enable light influence on the coupled magnetic and ferroelectric orders at a coherent interface of the magnet-in-ferroelectric materials. To achieve such potential, we surmise the following three design parameters: 1) magnet-in-ferroelectric crystals with the coherent interface to exhibit photoresponse; 2) coupling of photomagnetism and electro-optic effects with the stimuli response; and 3) piezoelectric induced interlayer magnetic coupling effect. In this context, two-dimensional (2D) layered magnetic materials offer an ideal platform for stimuli-dependent magnetic modulation due to their inter- and intralayer coupling and unique symmetry-tailored anisotropy (10–14). However, combining ferroelectric and magnetic phases in the same lattice remains a challenge due to its crystallographically incommensurate and dissimilar material nature (10, 15–17). Here, we grow molecular layered magnet-in-ferroelectric crystals for the investigation of photomagnetoelectricity (Fig. 1). The 2D magnetic $Cr(pyz)2{\cdot}xLiCl{\cdot}yTHF$ (LCPC) is selected as the magnetic component due to its excellent stimuli-dependent interlayer magnetic coupling while exhibiting high saturation magnetization of 20 emu/g and T_c above 415 K (18–20) (*SI Appendix*, Fig. S1). We select molecular imidazolium perchlorate ($ImClO_4$) ferroelectrics due to its high piezoelectric coefficient (d_{33} = 38.8 pm/V), optical transparency, and ferroelectricity with T_c of 382 K (21–24). A universal solution-based growth of molecular magnet-in-ferroelectric solids is presented as a different pathway to integrate the preformed layer magnet with molecular ferroelectric crystal.

Results

The schematic diagram of Fig. 1*A* depicts the growth of the layered magnetic LCPC-in-ferroelectric $ImClO_4$ matrix for the formation of LCPC-in-IM heterocrystals. Fig. 1*B* illustrates the schematic diagram of the LCPC-in-IM heterojunction structure. As shown in the structural diagram of LCPC-in-IM heterocrystals, we can observe that the coherent growth along the layered interface of LCPC. As shown in Fig. 1*C*, the π–π interaction between the pyrazine and imidazolium rings further facilitates the growth of $ImClO_4$ crystal on the LCPC. As a result of the π–π interactions and lattice compatibility, the growth of $ImClO_4$ matrix is parallel to the LCPC layered structure. Furthermore, we

Author affiliations: [a]Department of Materials Science and Engineering, University of Maryland, College Park, MD 20742; [b]Department of Chemistry, Virginia Tech, Blacksburg, VA 24060; [c]Department of Physics, Northeastern University, Boston, MA 02115; [d]Department of Materials and Science Engineering, Virginia Tech, Blacksburg, VA 24060; and [e]Department of Chemical and Biomolecular Engineering, University of Maryland, College Park, MD 20742

Author contributions: S.R. designed research; Z.W., Q.W., W.G., A.C., and A.I. performed research; Z.W., T.J.W., Q.Y., and L.Q. analyzed data; and Z.W. wrote the paper.

The authors declare no competing interest.

This article is a PNAS Direct Submission.

[1]To whom correspondence may be addressed. Email: sren@umd.edu.

This article contains supporting information online at https://www.pnas.org/lookup/suppl/doi:10.1073/pnas.2322361121/-/DCSupplemental.

Published April 16, 2024.

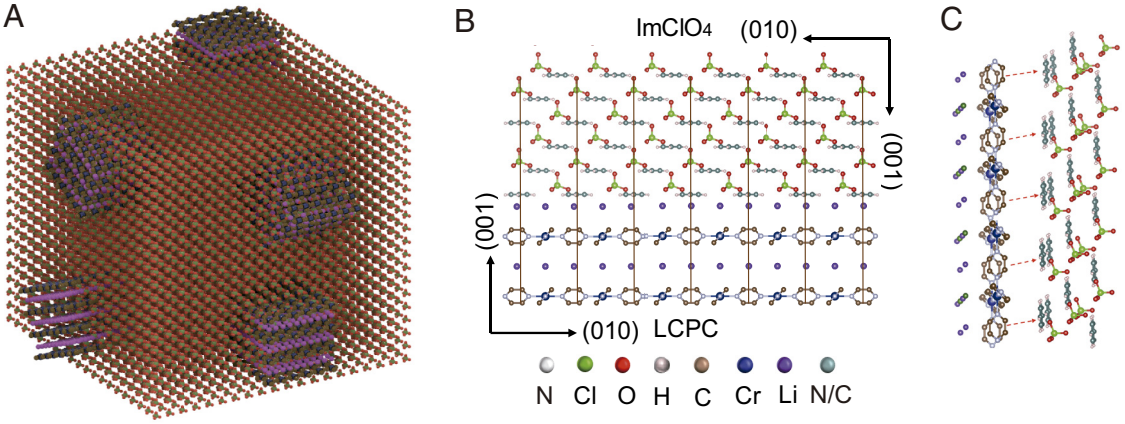

Fig. 1. (*A*) Schematic diagram of the three-dimensional structure of LCPC-in-IM heterocrystals. (*B*) Modeling of $ImClO_4$ and LCPC crystal structure and their interface. (*C*) Schematic diagram of π–π interaction and binding energy calculation structure of LCPC-in-IM heterocrystals. The hydrogen atom within the pyrazine ring has been omitted.

also calculated the interface binding energy between LCPC and $ImClO_4$. According to the calculation results, we found that the binding energy per area is around 30 meV/Angstrom^2. This indicates that LCPC is highly suitable for the growth-in-$ImClO_4$, which also ensures the perseverance of its ferroelectric properties. By introducing LCPC in $ImClO_4$ crystals, LCPC-in-IM simultaneously possesses both ferroelectric and magnetic properties. The LCPC-in-IM crystals exhibit a saturation polarization of 4.2 μC/cm^2 and a coercive field of 3.58 kV/cm. In comparison, the saturation magnetization is 0.75 emu/g, accompanied by a coercive field of 111 Oe. Notably, such molecular heterocrystals exhibit room-temperature magnetism, ferroelectricity, and magnetoelectric and photomagnetic coupling effects. The magnetization of LCPC-in-IM heterocrystals can be modulated by both light and electric fields. Under an illumination of 70 mW/cm^2, the magnetization reaches 0.015 emu/g. Simultaneously, the magnetoelectric (ME) coupling coefficient is 3.2×10^{-5} (A/m)/V. Using spectroscopy and diffraction techniques, we reveal a coherent interface at layered magnet-in-ferroelectrics that bridges photon, magnetic and electric orders to trigger unusual photomultiferroic properties. The crystallography analysis suggests the ferroelectric field effect on the piezoelectric $ImClO_4$ matrix effectively modulates the spin polarization of LCPC, leading to the photomagnetoelectricity of molecular heterocrystals at room temperature.

As shown in Fig. 2*A*, LCPC-in-IM heterocrystals exhibit a complete change of color while $ImClO_4$ presents itself as a transparent crystal and LCPC is characterized by its appearance as a black powder. A discernible deepening of the light reddish color is evident in optical photographs of LCPC-in-IM heterocrystals. As shown in Fig. 2*B*, the absorption spectrum analysis of $ImClO_4$ crystals demonstrates notable absorption characteristics primarily below 320 nm. Conversely, LCPC shows a pronounced absorption of the visible light with an absorption peak around 480 nm. The absorption spectrum of the LCPC-in-IM heterocrystals extends its coverage not only across the visible range from 400 to 900 nm but also exhibits pronounced absorption in the range below 350 nm. The introduction of LCPC into LCPC-in-IM heterocrystals engenders a similar absorption behavior for the visible light at the visible range with absorption peak appearing at approximately 480 nm. This observation provides further compelling evidence of the integration of LCPC within the $ImClO_4$ crystal. As shown in Fig. 2 *C* and *D*, LCPC-in-IM heterocrystals maintain its ferroelectricity after introducing LCPC in $ImClO_4$ crystals. Simultaneously, the integration of LCPC within the $ImClO_4$ crystal introduces ferromagnetic properties to the heterocrystals. However, the ferromagnetic characteristics of the LCPC-in-IM heterocrystals exhibit a significant reduction in both saturation magnetization and coercivity compared to LCPC. The saturation magnetization of the LCPC-in-IM heterocrystals is 0.75 emu/g, accompanied by a coercivity of 111 Oe. In contrast, the saturation magnetization of LCPC is 20 emu/g with a coercivity of 8,300 Oe (*SI Appendix*, Fig. S1). This observed diminishment in magnetic properties could be attributed to the crystallization of a portion of $ImClO_4$ within the interlayer of LCPC. LCPC's magnetism is highly susceptible to interlayer coupling (18). As illustrated in Fig. 2*E*, a substantial quantity of lamellar structures became evident on the crystal's surface, indicating a form embedded within the crystal. Furthermore, through energy dispersive X-ray spectroscopy (EDS) mapping of scanning electron microscope (SEM) image, we observe that these lamellar structures contain chromium (Cr) elements (Fig. 2*E* and *SI Appendix*, Fig. S3). This further underscores the coexistence of $ImClO_4$ and LCPC. In Fig. 2*E* and *SI Appendix*, Figs. S4 and S5, transmission electron microscope (TEM) imaging and EDS mapping of LCPC-in-IM heterocrystals are depicted. Both Cr and Cl elements are observed in LCPC-in-IM heterocrystals. It is noteworthy that the distribution area of Cl elements surpasses that of Cr elements. This observation suggests that within the LCPC-in-IM heterocrystals, the LCPC is enveloped within the $ImClO_4$ crystals. As shown in Fig. 2*F*, a high-resolution transmission electron microscope (HRTEM) image of LCPC-in-IM heterocrystals reveals distinct lattice spacing between the yellow and red regions. The lattice spacing in the yellow box measures 1.69 Å, corresponding to the (105) crystal plane of LCPC. In contrast, the lattice pitch in the red region is measured at 2.94 Å, aligning with the (111) of $ImClO_4$. This observation further substantiates the formation of LCPC-in-IM heterocrystals. The differing lattice spacings indicate the coexistence and integration of both $ImClO_4$ and LCPC phases within the heterocrystalline structure. As illustrated in Fig. 3*A*, crystalline phases of $ImClO_4$ are observed within the crystalline region of the LCPC layer in TEM image. This indicates that during the crystallization process of $ImClO_4$, due to the layered structure of LCPC, a portion of $ImClO_4$ infiltrates and crystallizes within the interlayers of LCPC. This significantly increases the interlayer spacing of LCPC. This may also account for the significant reduction

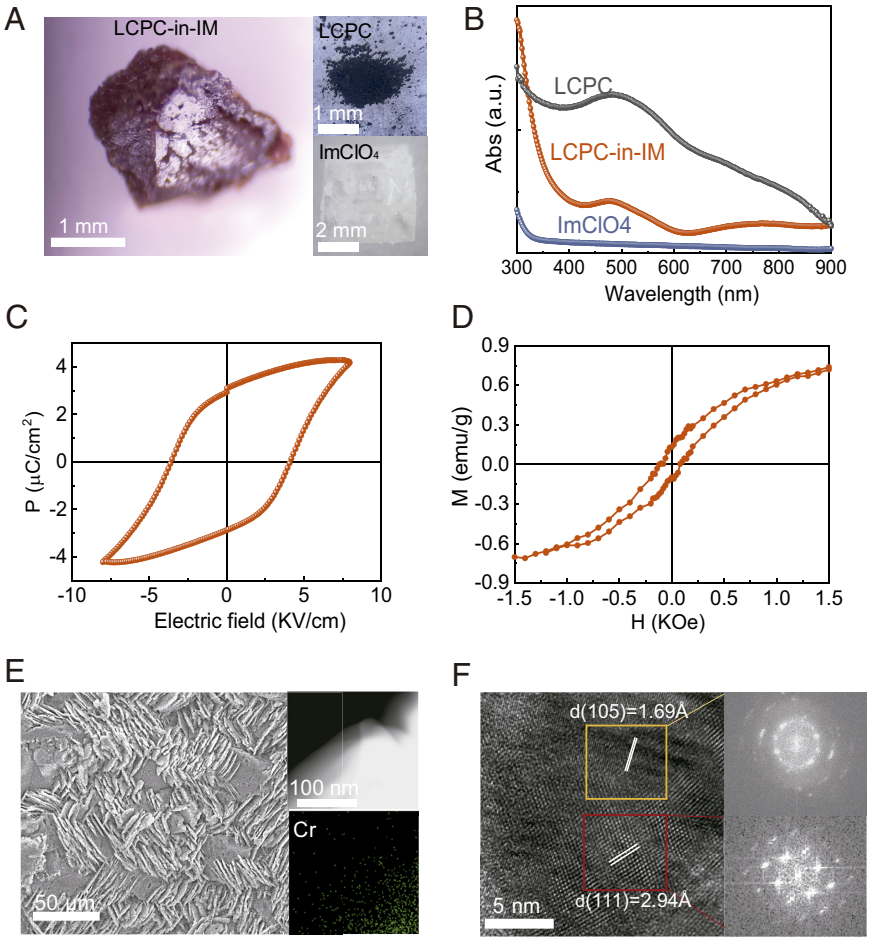

Fig. 2. (*A*) Optical photograph of $ImClO_4$, LCPC-in-IM heterocrystals, and LCPC. (*B*) Absorption spectrum of $ImClO_4$ crystals, LCPC, and LCPC-in-IM heterocrystals. (*C* and *D*) P-E Loop and Hysteresis loop of LCP-in-IM heterocrystals. P-E loop was tested at 200 Hz. (*E*) SEM image, TEM image, and EDS mapping of LCPC-in-IM hetercrytals. (*F*) HRTEM images and FFT image of LCPC-in-IM heterocrystals.

observed in the saturation magnetization and magnetic coercivity of LCPC-in-IM heterocrystals compared to LCPC.

We further validate the formation of the LCPC-in-IM heterocrystals by X-ray diffraction (XRD) analysis. The XRD pattern in Fig. 3*B* exhibits six main characteristic diffraction peaks of the LCPC-in-IM heterocrystals at 16.1°, 22.6°, 24.2°, 31.1°, 32.9°, and 35.5°, corresponding to the (100), (−110), (110), (111), (200), and (−210) planes, respectively. Hence, the incorporation of LCPC does not change the crystalline phase of $ImClO_4$ nor does it hinder the formation of electric dipoles and the overall ferroelectric properties. It is worth noting that two additional diffraction peaks appeared around 20.9° and 23.1° in LCPC-in-IM heterocrystals. This further indicates the formation of the magnet-in-ferroelectric heterocrystals. The full-width of half-maximum (FWHM) of the $ImClO_4$ and LCPC-in-IM (110) peaks are 0.283 and 0.436, respectively. Compared to the $ImClO_4$ crystal, the FWHM of the LCPC-in-IM heterocrystal has increased by 0.153. The full-width at FWHM of the LCPC-in-IM heterocrystals decreases due to the introduction of LCPC, resulting in a reduction in grain size. This reduction in crystallinity may be attributed to the crystallization of $ImClO_4$ within the interlayers of LCPC, coupled with a certain degree of lattice mismatch. *SI Appendix*, Fig. S6 shows the small-angle scattering X-ray diffraction (SAXRD) of $ImClO_4$, LCPC, and LCPC-in-IM heterocrystals. Both $ImClO_4$ and LCPC-in-IM exhibit three distinct diffraction peaks. Compared to $ImClO_4$, LCPC-in-IM heterocrystals exhibit two extra diffraction peaks, indicating the outgrowth of $ImClO_4$ matrix on the LCPC, forming the LCPC-in-IM heterocrystals. However, when the LCPC content exceeds 30 wt%, the crystallinity of LCPC-in-IM continuously deteriorates with the increasing LCPC content. Consequently, multiple crystalline diffraction peaks appear around 25° (*SI Appendix*, Fig. S7).

Meanwhile, the formation of LCPC-in-IM heterocrystals leads to the variations in the vibrational modes observed in FTIR (Fig. 3*C* and *SI Appendix*, Figs. S9 and S10). As shown in Fig. 3*C*, the N–H stretching vibration absorption peaks appeared at 3,522 cm^{-1} and 3,566 cm^{-1}, indicating a modification in the N–H vibrational mode of the imidazolium due to the heterocrystal structure. It is noteworthy that as the LCPC content increases from 10 to 20 wt%, the N–H stretching vibration absorption peak intensities around 3,522 cm^{-1} and 3,566 cm^{-1} are significantly enhanced by 13.6% and 17.5%, respectively (*SI Appendix*, Fig. S10). This indicates an increase in the N–H stretching vibrational mode within the LCPC-in-IM heterocrystals, which can be attributed to the increased interfacial coupling of LCPC, leading to an increase in the N–H stretching vibrational mode. Fig. 3 *D* and *E* show the Differential Scanning Calorimetry (DSC) and TGA curves of $ImClO_4$ and LCPC-in-IM heterocrystals, respectively. As shown in Fig. 3 *D* and *E* and *SI Appendix*, Fig. S11, the melting peaks of $ImClO_4$ and LCPC-in-IM heterocrystals are 485.5 K and 486 K, respectively. At the same time, as shown in Fig. 3*E*, the decomposition temperatures of LCPC-in-IM heterocrystals and $ImClO_4$ crystals are 501 K and 608 K, respectively. The decomposition temperature of LCPC-in-IM has decreased by approximately 107 K due to the presence of LCPC phase. This is attributed to the crystallization of $ImClO_4$ within the interlayers of LCPC and lattice mismatch, resulting in a reduction in crystallinity for LCPC-IM compared to $ImClO_4$. Consequently, this leads to a reduction in the thermal stability of LCPC-in-IM heterocrystals, as well as a decrease in both melting temperature (Tm) and

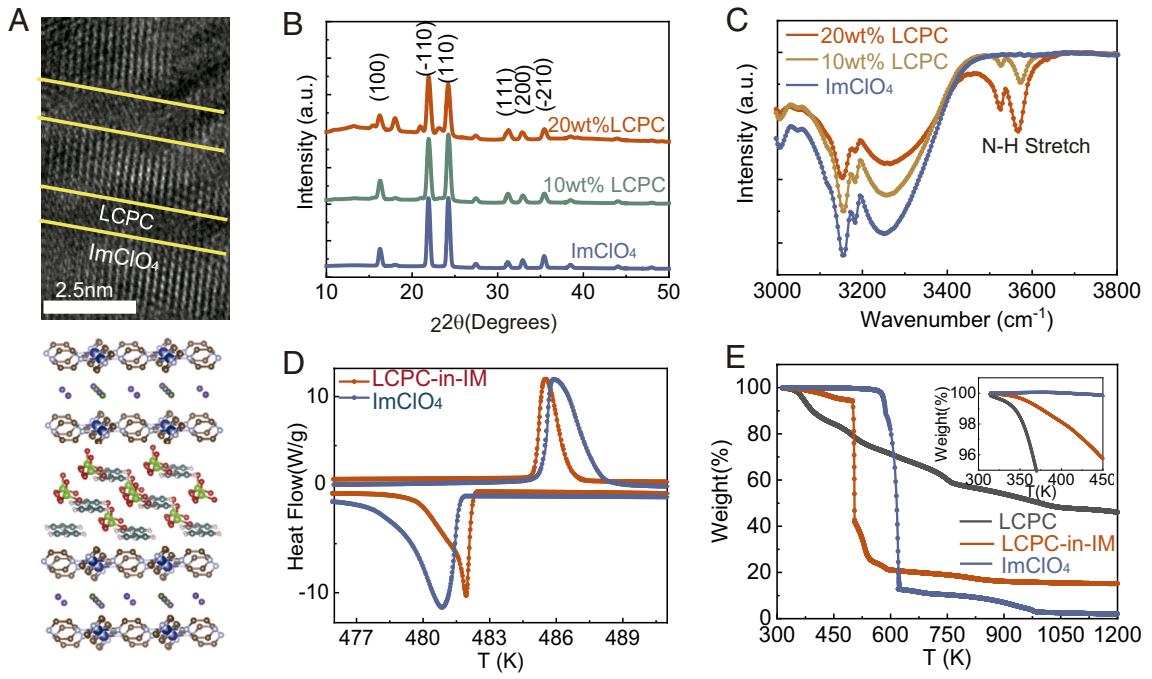

Fig. 3. (*A*) HRTEM images and schematic diagram of LCPC-in-IM heterocrystals. The hydrogen atom within the pyrazine ring has been omitted. (*B*) PXRD patterns of $ImClO_4$ crystals and LCPC-in-IM heterocrystals with 10 wt% and 20 wt% LCPC. (*C*) Fourier transform infrared spectroscopy (FTIR) spectra of $ImClO_4$ crystals and LCPC-in-IM heterocrystals with different mass rate of LCPC. (*D*) Differential scanning calorimetry (DSC) curves of $ImClO_4$ crystals and LCPC-in-IM heterocrystals. (*E*) TGA curves from 300 to 1,200 K.

decomposition temperature (Td). Additionally, as indicated in the Fig. 3 *D*, *Inset*, a decrease in mass is observed for LCPC-in-IM heterocrystals starting at 315 K. This is attributed to the gradual decomposition of LCPC, resulting in a reduction in overall mass for LCPC-in-IM heterocrystals. Furthermore, we also calculated the interface binding energy between LCPC and $ImClO_4$. According to the calculation results (*SI Appendix*, Fig. S8 and Table S1), we found that the binding energy per area is around 30 meV/Angstrom^2. This also indicates that the stability of the LCPC-in-IM heterocrystals is inferior compared to $ImClO_4$.

The high transmittance of $ImClO_4$ crystals within the visible wavelength range sets the stage for photomodulated magneto-electric coupling. Therefore, the photomagnetic effect is observed in the LCPC-in-IM heterocrystals. As demonstrated in Fig. 4*A*, the magnetization intensity displays a notable response to varying light intensities. It is evident from the graph that the magnetization intensity of the LCPC-in-IM heterocrystals increases from 0.002 emu/g to approximately 0.015 emu/g as the light intensity escalates from 2.5 mW/cm^2 to 70 mW/cm^2. Notably, the reversibility of light-modulated magnetization is clearly observed. To further corroborate the presence of the photomagnetic coupling effect in the LCPC-in-IM heterocrystals, we conducted measurements on the light intensity-dependent ferromagnetic resonance (FMR). As illustrated in Fig. 4*B*, the FMR field exhibits a decline with ascending light intensity. Specifically, the FMR field decreases from 1110 Oe to 200 Oe as the light intensity increases from 2.5 mW/cm^2 to 70 mW/cm^2 (Fig. 4*C*). This implies that either the magnetization or the anisotropy of the heterocrystals experiences a concurrent rise with the augmentation of light intensity (25–29). This further confirms the existence of photomagnetic coupling in LCPC-in-IM heterocrystals. As shown in *SI Appendix*, Fig. S12, the magnetization of LCPC remains unchanged under illumination compared to the dark. We did not observe photomagnetic effect in the LCPC, even when subjected to a light intensity as high as 70 mW/cm^2. This observation suggests that the photomagnetic effect in LCPC-in-IM heterocrystals could be attributed to their unique magnet-in-ferroelectric heterocrystal structure. Through an analysis of the frequency-dependent dielectric curves at varying light intensities, we recognize that the dielectric constant of LCPC and LCPC-in-IM heterocrystals experiences an increment with increasing light intensity (Fig. 4*D* and *SI Appendix*, Figs. S13–S15). This suggests that LCPC is capable of generating space charge and dipoles under illumination. Consequently, the light-induced charges and dipoles within LCPC engage in electrostatic interactions with the electric dipoles situated at the $ImClO_4$ interface, thereby influencing the electric polarization within $ImClO_4$ crystals. In response, $ImClO_4$ generates lattice strain as a result of piezoelectricity. Due to the distinctive heterocrystalline structure, the lattice strain of $ImClO_4$ effectively modulates the magnetic properties of LCPC, which exhibits high sensitivity to mechanical pressure. In Fig. 4*D*, *Inset*, a schematic representation of photomagnetic coupling is depicted, arising from light-induced interfacial lattice strain. It is evident from the diagram that LCPC undergoes charge generation upon exposure to light excitation. This photogenerated charge instigates an interfacial coupling phenomenon with the electric dipole situated at the $ImClO_4$ interface. The quantity of photogenerated charge is finely regulated by the intensity of incident light. Consequently, the efficacy of interfacial coupling between the photogenerated charge and electric dipole is contingent upon light intensity. This interfacial coupling event leads to the polarization of dipoles within the $ImClO_4$, inducing lattice strain. This, in turn, governs the interlayer magnetic coupling within LCPC through the piezoelectric effect. The phenomenon of photo-induced ferromagnetic–ferroelectric interface electrostatic interactions enables light-induced piezoelectric-tailored magnetism. Under the influence of light, the photogenerated charges or dipoles experience a redistribution owing to interfacial electrostatic interactions. This leads to the establishment of an electrostatic field, subsequently giving rise to the emergence of electrode polarization within the $ImClO_4$ crystals, leading to lattice

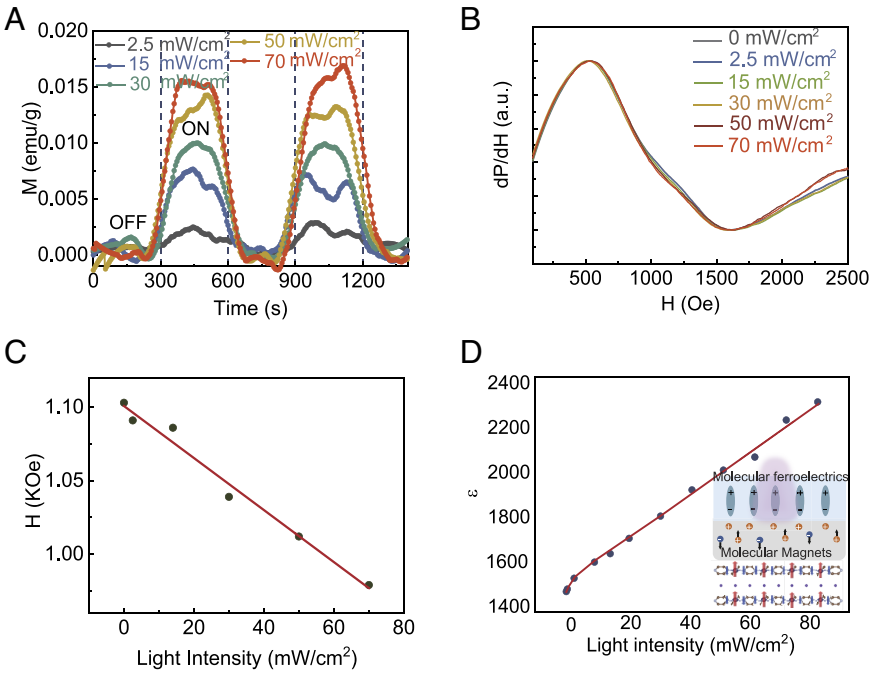

Fig. 4. (*A*) Illumination-dependent magnetization in LCPC-in-IM heterocrystals. (*B*) Illumination-dependent ferromagnetic resonance spectra in LCPC-in-IM heterocrystals. (*C*) Illumination-dependent ferromagnetic-resonance field shift in LCPC-in-IM heterocrystals. (*D*) Illumination-dependent dielectric constant of LCPC-in-IM heterocrystals. The illustration depicts a schematic diagram of interfacial electrostatic interactions at the LCPC and $ImClO_4$ crystals interface under illumination.

strain (30, 31). The interfacial lattice strain exerts pressure on the LCPC, resulting in a variation in the strength of interlayer magnetic coupling within the LCPC (12, 14, 18). Ultimately, this cascade of events culminates in the photomagnetic effect mediated by photo-induced interfacial electrostatic coupling in the LCPC-in-IM system.

To further confirm the photo-introduced interfacial lattice strain on the magnetic properties of LCPC-in-IM heterocrystals, we conducted measurements of the temperature- and electric-field-dependent magnetization intensity in LCPC-in-IM heterocrystals. As shown in Fig. 5*A*, the temperature-dependent magnetization reveals a coupling effect between ferroelectric polarization and spin polarization in the LCPC-in-IM heterocrystals. The red and blue curves in Fig. 5*A* represent the temperature-dependent magnetization of LCPC-in-IM heterocrystals and dielectric constant of $ImClO_4$ crystals, respectively. The black curve illustrates the temperature-dependent magnetization of LCPC. From the temperature-dependent magnetization curve of LCPC, we can observe that its Curie temperature (T_c) is around 415 K, while $ImClO_4$ exhibits a ferroelectric transition temperature of 382 K. This lays the foundation for the room temperature ME coupling. As shown in the red curve in Fig. 5*A*, this is evident in a noticeable reduction in magnetization by approximately 0.0024 emu/g (8% of magnetization at a 1,000 Oe external field) in the vicinity of the ferroelectric Curie temperature (T_c of 382 K). To further study the electric field–dependent piezoelectric-induced ME coupling effect, we measured the electric field–dependent FMR signal and magnetization of the LCPC-in-$ImClO_4$ heterocrystals. As shown in Fig. 5*B*, the ferromagnetic resonance field experiences a decrease from 1,040 Oe to 945 Oe when subjected to an electric field of 1,000 V/cm. This observation indicates that the magnetization or anisotropy of LCPC-in-IM is heightened under the influence of an electric field. In addition, it can be observed that the magnetization of LCPC-in-IM heterocrystals can be effectively tuned by an external electric field (Fig. 5*B*). At an electric field of 500 V/cm, the magnetization intensity can reach 0.016 emu/g. The ME coupling coefficient at 500 V/cm is 3.2×10^{-5} (A/m)/V. As the electric field increases to 2,000 V/cm and 3,200 V/cm, the corresponding ME coupling coefficients are 1.3×10^{-5} (A/m)/V and 1.28×10^{-5} (A/m)/V, respectively. Furthermore, as the electric field is further increased to 4,000 V/cm, the magnetization of heterocrystals is further enhanced and can reach 0.048 emu/g. It means that ME coupling coefficient drops to 1.2×10^{-5} (A/m)/V at 4,000 V/cm. This indicates that with the increase in electric field, the ME coupling coefficient decreases.

Fig. 5*D* illustrates the schematic diagram of the interlayer spacing compression in the LCPC-in-IM heterocrystals induced by electric field or light-induced lattice strain in the $ImClO_4$ lattice. From Fig. 5*D*, it can be observed that the lattice strain induced by light or an electric field in the $ImClO_4$ lattice results in a significant reduction in the interlayer spacing of LCPC due to compression. As a two-dimensional layered magnet, the magnetic properties of LCPC arise from the magnetic exchange interaction between the antiparallel spins of Cr and N from pyrazine which exhibits a pressure-dependent interlayer magnetic coupling behavior. Lattice modifications can change the interlayer coupling effect, thus regulating the strength of magnetic interactions between Cr and pyrazine. Meanwhile, as a piezoelectric material, the lattice constant of $ImClO_4$ can be tuned by an external electric field. The electric field-induced lattice strain in $ImClO_4$ exerts pressure on LCPC within the $ImClO_4$ matrix. Therefore, lattice strain induced by an external electric field can effectively modulate the magnetism of LCPC. As the pressure continues to increase, the interlayer contraction due to pressure becomes increasingly challenging. This leads to a gradual weakening of the change in magnetization intensity caused by pressure. This may also be a reason for the gradual decrease in the magneto-electric coupling coefficient with the applied external electric field. In order to confirm the electric field modulation of the $ImClO_4$ lattice structure, we conducted electric field-dependent XRD measurements of LCPC-in-IM heterocrystals. As the electric field intensity gradually increased from 1,000 V/cm to 5,000 V/cm, the (–110) peak of LCPC-in-IM heterocrystals shifted from 22.61°to 22.57° (Fig. 5*E* and *SI Appendix*, Fig. S21). This shift of XRD peaks indicates an expansion of the lattice, suggesting an increase in the $ImClO_4$ lattice. As shown in Fig. 5*F*, under a 5 kV/cm electric field, the lattice constant of $ImClO_4$ can increase by approximately 2‰. This indicates that the applied electric field causes the expansion of the $ImClO_4$ lattice within LCPC-in-IM heterocrystals. The light-induced interface-enhanced electrostatic coupling effect is further amplified by the electrostatic field originating from the redistribution of photogenerated charges and dipoles. This

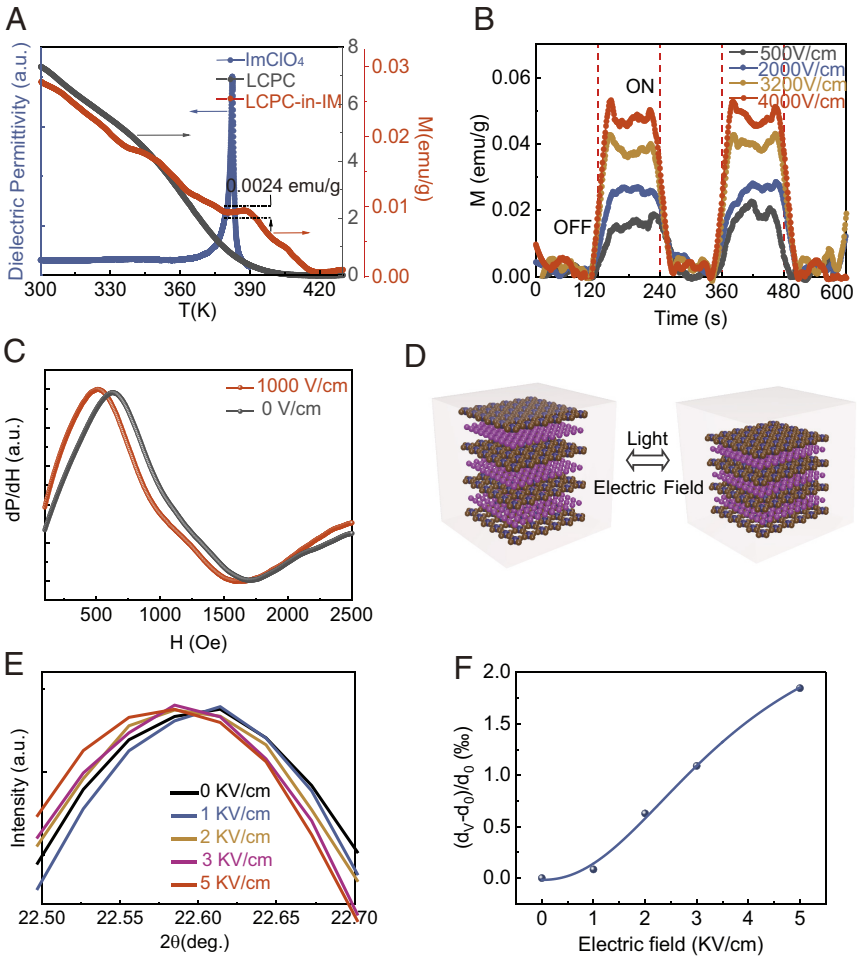

Fig. 5. (*A*) The temperature-dependent magnetization and dielectric properties of LCPC-in-IM heterocrystals, $ImClO_4$, and LCPC. (*B* and *C*) Electric field tuning of ferromagnetic resonance spectra and magnetization in LCPC-in-IM heterocrystals. (*D*) Schematic diagram of enhanced interlayer coupling in LCPC induced by light- or electric field–induced ferroelectric lattice strain. (*E* and *F*) Electric field–dependent XRD (−110) peak shift of LCPC-in-IM heterocrystals.

induces lattice expansion within the $ImClO_4$ crystal, exerting pressure at the interface between LCPC and $ImClO_4$. The diminished interlayer spacing of LCPC under external pressure heightens the interlayer magnetic exchange interaction between Cr and pyrazine, consequently augmenting the overall magnetization strength of LCPC. The introduction of external electric fields generates thermal energy due to the induced polarization change, which may disrupt the long-range ferromagnetic order in ferromagnetic materials, leading to a decrease in magnetization rather than an increase (32–34). However, in LCPC-in-IM heterocrystals crystals, the application of an external electric field can enhance their magnetization. This suggests that the thermal energy introduced by the external electric field is not the dominant factor in altering the magnetization. Furthermore, under illumination, the magnetization is observed to increase rather than decrease, indicating that the enhancement of magnetization under both external electric fields and light is attributed to the strengthening of interlayer ferromagnetic coupling in LCPC induced by lattice expansion in the IM ferroelectric crystals. Therefore, the light-induced interfacial electrostatic coupling emerges as the pivotal mechanism driving the generation of photomagnetic coupling in LCPC-in-IM heterocrystals.

In summary, we report a universal solution-based growth of layered magnet-in-ferroelectric crystals to introduce room temperature molecular photomultiferroic LCPC-in-IM heterocrystals. Due to the π–π stacking interaction of pyrazine and imidazolium rings, $ImClO_4$ forms a heterojunction interface with LCPC during epitaxial growth without altering the ferroelectric properties. The formation of the heterojunction interface leads to the emergence of two crystalline peaks near 20.9° and 23.1° in the LCPC-in-IM crystal, indicating the presence of an additional crystalline phase in LCPC-in-IM. However, the LCPC-in-IM interface introduces a reduction of 0.5 K in the melting temperature as compared to that of parent crystals. The light-induced lattice interactions for the photomagnetoelectricity are observed on the LCPC-in-IM heterocrystals. The interfacial coupling initiates dipole polarization within $ImClO_4$, thereby inducing lattice strain. This strain, in consequence, regulates the interlayer magnetic coupling within LCPC via the piezoelectric effect. Ultimately, this orchestrated sequence of events leads to the manifestation of the photomagnetic coupling effect. Based on the unique pressure-dependent interlayer magnetic coupling effect and the lattice modulation of ferroelectric crystals by light, we demonstrate a coupled effect between photon, charge, and spin orders.

Materials and Methods

$Cr(pyz)_2Cl_2$ Precursor Synthesis. The $Cr(pyz)_2Cl_2$ precursor was synthesized through a solvothermal method outlined in the literature. Specifically, 22.1 grams $CrCl_2$ and 10 grams pyrazine were carefully combined in a 100-mL Teflon-lined stainless-steel autoclave reactor. The reactor was heated to 200 °C, maintained for 24 h, and gradually cooled to room temperature.

Solvation Lithiation for $Cr(pyz)_2$·xLiCl. A mixture of 231.3 mg 1,2-dihydroacenaphtylene and 104 mg lithium in 8 mL THF solvent was stirred for three hours. The filtered solution was then introduced into a 20-mL glass vessel containing 5 mL THF solution, along with 200 mg of the $Cr(pyz)_2Cl_2$ precursor. After a week of stirring, the product was washed with 15 mL THF solvent two or three times and vacuum-dried. The resulting powder was annealed in a glove box using a hotplate for 5 to 10 min to remove any residual THF solvent.

$ImClO_4$ Synthesis. $ImClO_4$ crystals were synthesized by gradually evaporating an aqueous solution containing imidazolium chloride and perchloric acid in a 1:1 molar ratio. The resulting $ImClO_4$ crystals were then dissolved in anhydrous ethanol to prepare a saturated solution with a concentration of 64 mg/mL.

Preparation of Cocrystals. LCPC powder with varying mass ratios was introduced into a solution of $ImClO_4$ (64 mg/mL). After 5 min of ultrasonication, the mixture was stirred at room temperature for 0.5 h. Crystallization occurred through slow evaporation in a 20 mL vial. To prevent the oxidation of LCPC, all preparation processes were conducted inside a glove box.

Magnetic and FMR Measurements under Illumination and Electric Field. Light intensity, electric field, and temperature-dependent magnetic properties were assessed using a vibrating sample magnetometer–specifically, the MicroSense EZ7-380V model. FMR experiments involved microwave (MW) irradiation, utilizing a continuous wave (CW) FMR system. This system employed a CW broad-band MW source (Agilent N5172B-520; 1 to 19 GHz), connected to a coplanar waveguide (CPW) with the sample positioned in close proximity. A power-adjustable 405 nm laser was employed as the excitation light source.

Electrical and Dielectric Measurements. Polarization-electric field (P-E) hysteresis loops were recorded using a Precision LC Ferroelectric Tester, enhanced with a high voltage interface and a Trek 609B high voltage amplifier (Radiant Technologies Inc., USA). The measurement setup allowed for precise control and analysis of the polarization-electric field behavior in the sample. Light intensity–dependent dielectric constant was measured using an Agilent 4294 A impedance analyzer.

Thermal Analysis and UV–Vis Absorption Measurement. Thermal transitions were identified through a Perkin Elmer (Shelton, CT) DSC 7 differential scanning calorimeter, with experiments conducted at a heating rate of 5 °C min^{-1}. The assessment of thermal degradation was performed using a TGA (SDT Q600, TA Instruments., USA) under a N_2 atmosphere. UV–Vis absorption spectra were acquired employing an Agilent Cary 7000 UV–Vis–near-IR spectrophotometer.

Computational Methods. Calculations were performed by using the density functional theory (DFT), as implemented in the Vienna Ab initio Simulation Package. To include the many-body effect of Cr atoms, DFT + U method was applied with U = 4.0 eV and J = 0 eV. The projector-augmented-wave method and a plane-wave basis set were used. A plane-wave cutoff energy of 520 eV and 2 × 1 × 1 Monkhorst–Pack k-point grid was used for all calculations. The matching interface structures were generated based on the Zur Super Lattice method, as implemented in pymatgen.

Data, Materials, and Software Availability. All study data are included in the article and/or *SI Appendix*.

ACKNOWLEDGMENTS. The US Department of Energy, Office of Basic Energy Sciences, Division of Materials Sciences and Engineering supports S.R. under Award DE-SC0024796. W.G. and Q.Y. acknowledge funding support from the U.S. Department of Energy, Office of Science, Basic Energy Sciences, under Award No. DE-SC0023664. This research used resources of the National Energy Research Scientific Computing Center (NERSC), a U.S. Department of Energy Office of Science User Facility located at Lawrence Berkeley National Laboratory, operated under Contract No. DE-AC02-05CH11231 using NERSC award BES-ERCAP0029544.

1. M. Bibes, Nanoferronics is a winning combination. *Nat. Mater.* **11**, 354–357 (2012).
2. Y.-H. Chu *et al.*, Electric-field control of local ferromagnetism using a magnetoelectric multiferroic. *Nat. Mater.* **7**, 478–482 (2008).
3. J. T. Heron *et al.*, Deterministic switching of ferromagnetism at room temperature using an electric field. *Nature* **516**, 370–373 (2014).
4. J.-M. Hu, L.-Q. Chen, C.-W. Nan, Multiferroic heterostructures integrating ferroelectric and magnetic materials. *Adv. Mater.* **28**, 15–39 (2016).
5. Y.-L. Huang *et al.*, Manipulating magnetoelectric energy landscape in multiferroics. *Nat. Commun.* **11**, 2836 (2020).
6. N. A. Spaldin, R. Ramesh, Advances in magnetoelectric multiferroics. *Nat. Mater.* **18**, 203–212 (2019).
7. A. Dmitriyeva *et al.*, Magnetoelectric coupling at the Ni/Hf0.5Zr0.5O2 interface. *ACS Nano* **15**, 14891–14902 (2021).
8. S. Lindemann *et al.*, Low-voltage magnetoelectric coupling in membrane heterostructures. *Sci. Adv.* **7**, eabh2294 (2021).
9. B. Peng *et al.*, Large in-plane piezo-strain enhanced voltage control of magnetic anisotropy in Si-compatible multiferroic thin films. *Mater. Horiz.* **9**, 3013–3021 (2022).
10. M. N. Akhtar, M. A. AlDamen, C. D. McMillen, A. Escuer, J. Mayans, Exploring the role of intramolecular interactions in the suppression of quantum tunneling of the magnetization in a 3d–4f single-molecule magnet. *Inorg. Chem.* **60**, 9302–9308 (2021).
11. L. Hu *et al.*, Polymer-buried van der Waals magnets for promising wearable room-temperature spintronics. *Mater. Horiz.* **8**, 3306–3314 (2021).
12. T. Li *et al.*, Pressure-controlled interlayer magnetism in atomically thin CrI_3. *Nat. Mater.* **18**, 1303–1308 (2019).
13. C. Moulsdale, A. Knothe, V. Fal'ko, Engineering of the topological magnetic moment of electrons in bilayer graphene using strain and electrical bias. *Phys. Rev. B* **101**, 085118 (2020).
14. T. Song *et al.*, Switching 2D magnetic states via pressure tuning of layer stacking. *Nat. Mater.* **18**, 1298–1302 (2019).
15. C. Boskovic *et al.*, Ferromagnetic and antiferromagnetic intermolecular interactions in a new family of Mn_4 complexes with an energy barrier to magnetization reversal. *J. Am. Chem. Soc.* **125**, 14046–14058 (2003).
16. J. H. Lee *et al.*, A strong ferroelectric ferromagnet created by means of spin–lattice coupling. *Nature* **466**, 954–958 (2010).
17. A. Prescimone *et al.*, [Mn6] under Pressure: A combined crystallographic and magnetic study. *Angew. Chem. Int. Ed. Engl.* **47**, 2828–2831 (2008).
18. Y. Huang *et al.*, Pressure-controlled magnetism in 2D molecular layers. *Nat. Commun.* **14**, 3186 (2023).
19. Y. Huang *et al.*, Chemical tuning meets 2D molecular magnets. *Adv. Mater.* **35**, 2208919 (2023).
20. P. Perlepe *et al.*, Metal-organic magnets with large coercivity and ordering temperatures up to 242 °C. *Science* **370**, 587–592 (2020).
21. Y. Huang *et al.*, Proton-controlled molecular ionic ferroelectrics. *Nat. Commun.* **14**, 5041 (2023).
22. W. Li *et al.*, The strong electrocaloric effect in molecular ferroelectric ImClO4 with ultrahigh electrocaloric strength. *J. Mater. Chem. A* **8**, 16189–16194 (2020).
23. Y. Zhang *et al.*, A molecular ferroelectric thin film of imidazolium perchlorate that shows superior electromechanical coupling. *Angew. Chem. Int. Ed. Engl.* **53**, 5064–5068 (2014).
24. Z. Zhang *et al.*, Tunable electroresistance and electro-optic effects of transparent molecular ferroelectrics. *Sci. Adv.* **3**, e1701008 (2017).
25. A. C. Chavez *et al.*, Voltage-controlled ferromagnetic resonance of dipole-coupled Co_{40} $Fe_{40}B_{20}$ nanoellipses. *Phys. Rev. Appl.* **12**, 044071 (2019).
26. D. Markó *et al.*, Tunable ferromagnetic resonance in coupled trilayers with crossed in-plane and perpendicular magnetic anisotropies. *Appl. Phys. Lett.* **115**, 082401 (2019).
27. P. Pathak, A. Kumar, D. J. P. R. A. Mallick, Light-induced ferromagnetic resonance shift in magnetoelectric heterostructure. *Phys. Rev. Appl.* **20**, 044055 (2023).
28. R. Yu *et al.*, Nonvolatile electric-field control of ferromagnetic resonance and spin pumping in Pt/YIG at room temperature. *Adv. Electron. Mater.* **5**, 1800663 (2019).
29. M. Zheng, T. Usami, T. J. N. A. M. Taniyama, Shear-strain-mediated large nonvolatile tuning of ferromagnetic resonance by an electric field in multiferroic heterostructures. *NPG Asia Mater.* **13**, 7 (2021).
30. J. Eom *et al.*, Voltage control of magnetism in $Fe_{3-x}GeTe_2$/In_2Se_3 van der Waals ferromagnetic/ferroelectric heterostructures. *Nat. Commun.* **14**, 5605 (2023).
31. S. Saha *et al.*, Strain transfer in ferroelectric-ferrimagnetic magnetoelectric composite. *Phys. Rev. B* **103**, L140106 (2021).
32. Y. Cao *et al.*, Polar bear hair inspired supra-photothermal promoted water splitting. *ACS Mater. Lett.* **4**, 1912–1920 (2022).
33. B. Dai *et al.*, Recent advances in efficient photocatalysis via modulation of electric and magnetic fields and reactive phase control. *Adv. Mater.* **35**, 2210914 (2023).
34. L. Gao *et al.*, Operando unraveling photothermal-promoted dynamic active-sites generation in $NiFe_2O_4$ for markedly enhanced oxygen evolution. *Proc. Natl. Acad. Sci. U.S.A.* **118**, e2023421118 (2021).